

When does the onset of multiple stellar populations in star clusters occur-II: No evidence of multiple stellar populations in Lindsay 113

CHENGYUAN LI,^{1,2} YUE WANG,² AND ANTONINO P. MILONE³

¹*School of Physics and Astronomy, Sun Yat-sen University, Zhuhai 519082, China*

²*Key Laboratory for Optical Astronomy, National Astronomical Observatories, Chinese Academy of Sciences, 20A Datun Road, Beijing 100101, China*

³*Dipartimento di Fisica e Astronomia “Galileo Galilei”, Univ. di Padova, Vicolo dell’Osservatorio 3, Padova, IT-35122*

Submitted to ApJ

ABSTRACT

The presence of multiple populations (MPs) in almost all globular clusters (GCs) older than ~ 10 Gyr, has caught lots of attention. Recently, cumulative evidence indicates that extragalactic GCs that are older than 2 Gyr, seem to also harbor MPs, however, those that are younger than 2 Gyr do not. These observations seem to imply that age is a primary property that controls the presence of MPs in star clusters. However, because of the lack of studies of intermediate-age (~ 2 – 6 Gyr-old), low mass clusters, it is unclear if the cluster mass, in addition to age, also plays a role in the occurrence of MPs. In this work, we studied a ~ 4 Gyr-old, low mass ($\sim 23,000 M_{\odot}$) cluster, Lindsay-113, in the Small Magellanic Cloud. Using *Hubble Space Telescope* photometry, we find that the width of the red-giant branch in this cluster, when measured in a specific color index that is sensitive to star-to-star chemical variations, can be adequately explained by a “simple” stellar population model with some possible noises contributed from measurement uncertainty, photometric artifact, as well as differential reddening. The comparison of observations with predictions from synthetic spectra indicates that the internal chemical spread in nitrogen abundance, which is a signature of MPs, would not exceed 0.2 dex. Since Lindsay 113 is significantly older than other GCs with MPs, we suggest that the onset of MPs is likely determined by the combination of cluster age and mass.

Keywords: globular clusters: individual: Lindsay-113 – Hertzsprung-Russell and C-M diagrams

1. INTRODUCTION

The detection of chemical spread in almost all Galactic globular clusters (GCs, older than ~ 10 Gyr) has made the notion of star clusters as simple stellar populations (SSPs) a view of the past. The star-to-star variations in the abundances of some light elements along different evolutionary phase (e.g., Carretta et al. 2009; Marino et al. 2009; Pancino et al. 2017; Wang et al. 2017) in GCs strongly indicates that they are multiple stellar populations (MPs) rather than SSPs. In photometry, MPs are responsible for distinctive features along with the entire color-magnitude diagram (CMD), including multiple main sequences (MSs, Piotto et al. 2007),

subgiant branches (SGBs, Villanova et al. 2007), red-giant branches (RGBs, Marino et al. 2008; Piotto et al. 2015), and also their combinations. Milone et al. (2017) has developed a pseudo-two-color diagram with a suitable combination of multiple passbands observed through the *Hubble Space Telescope* (*HST*). This diagram, which is called the “chromosome map” of GCs, is proved an effective tool for detecting different stellar populations in GCs.

Numerous studies show that MPs are also present in extragalactic clusters. Letarte et al. (2006) have studied detailed chemical abundances among stars in three GCs of the Fornax dwarf spheroidal (dSph) galaxy. They find that the chemical pattern of Fornax dSph GCs is similar to those of Galactic GCs. This conclusion was underpinned by Larsen et al. (2014), in which they report the presence of nitrogen (N) variations among RGB stars for the same clusters, using the UV-optical-

Infrared photometry based on the *HST*. MPs with different chemical composition were also detected in clusters in the Small and the Large Magellanic Cloud (SMC and LMC) by using both photometry (Dalessandro et al. 2016; Niederhofer et al. 2017; Martocchia et al. 2018; Lagioia et al. 2019; Li & de Grijs 2019) and spectroscopy (Mucciarelli et al. 2009; Hollyhead et al. 2019).

To explain the origin of MPs, a significant fraction of models draw on self-pollution of the intra-cluster gas, which would be occurring during a clusters early evolution. Different scenarios invoke different stellar sources for chemical enrichment (e.g., Decressin et al. 2007; D’Ercole et al. 2008; de Mink et al. 2009). However, detail explorations show that these scenarios would inevitably encounter problems when compare with observations (Bastian et al. 2015). Recently, some scenarios also suggest a significant contribution from external accretion (Li et al. 2016; Hong et al. 2017; Bekki 2019). All these scenarios would suggest that a significant fraction of gas content or young stellar objects can occur in advanced, massive clusters, which still remains controversial (Bastian & Strader 2014, however, For & Bekki (2017)).

One possible explanation is that stellar chemical anomalies are produced inside low mass stars and were present when they were sufficiently evolved (e.g. Briley et al. 1989; Cavallo et al. 1996, 1998). The MPs in GCs might be caused by stellar evolutionary processes such as the first dredge-up and the Sweigart-Mengel mixing (Sweigart & Mengel 1979). The findings of chemical anomalies among less-evolved MS stars (e.g. Cannon et al. 1998) have challenged these scenarios, because they are not hot enough for producing the observed chemical enrichment pattern. Alternatively, Jiang et al. (2014) proposed that stars with anomalous abundances in GCs might be the products of binary interactions. Recently Bastian & Lardo (2018) suggest that MPs may be built with the help of some non-standard stellar evolutionary effects. They claim that a strong magnetic field associated with low mass stars may play a significant role in it, as only low mass stars that are magnetically braked exhibit obvious patterns of chemical variations. This scenario, although speculative, was supported by the evidence that clusters younger than ~ 2 Gyr both in the Magellanic Clouds and in the Milky Way exhibit extended MS turnoffs (e.g., Milone et al. 2009), and clusters younger than ~ 700 Myr show split or broadened MSs (e.g., Li et al. 2017; Cordoni et al. 2018).

Clusters younger than ~ 2 Gyr do not show evidence for light-element variations (e.g., Mucciarelli et al. 2014; Martocchia et al. 2017; Zhang et al. 2018), hence they

do not host MPs with a different chemical composition. Indeed the eMSTOs and the multiple MSs of these young clusters are mainly due to the stellar rotation (e.g., Yang et al. 2013; D’Antona et al. 2017; Georgy et al. 2019), as demonstrated by direct spectroscopic measurements of stellar rotation in MS and eMSTO stars (Dupree et al. 2017; Marino et al. 2018a,b; Sun et al. 2019).

The “self-enrichment” or “external accretion” scenarios suggest that the total cluster mass would be the dominant property which defines the presence of MPs. On the other hand, “stellar evolutionary” scenarios would imply that MPs can only be observed in sufficiently evolved stellar systems. Therefore age is the key factor determining the occurrence of MPs. For old GCs in the Milky Way, observations strongly indicate that the significance of the MPs depends on the cluster’s total mass (e.g., Carretta et al. 2010; Milone et al. 2017, 2018). In these studies, MPs’ phenomenon systematically increases in both incidence and complexity with increasing cluster mass.

Only one old GC, Ruprecht 106 (Rup 106), was identified as a convincing sample of SSP GC (Villanova et al. 2013; Dotter et al. 2018). However, MPs are also detected in GCs less massive than Rup 106 (e.g., NGC 6535, Bragaglia et al. 2017). A similar correlation was also present in clusters with ages between 2 to 10 Gyr as well (Chantereau et al. 2019). According to Chantereau et al. (2019), there seems to be a minimum threshold mass of about $30,000 M_{\odot}$ for the appearance of MPs. However, the fact that their younger counterparts with comparable total masses do not exhibit MPs, has led to the argument that age is the major factor determining the presence of MPs.

Unfortunately, stellar populations in clusters of 2–6 Gyr-old are yet less studied. So far only six clusters in this age range were explored in terms of their stellar populations (Martocchia et al. 2018; Chantereau et al. 2019; Hollyhead et al. 2019; Li & de Grijs 2019; Martocchia et al. 2019). Among these clusters, NGC 1978, NGC 2121 and Hodge 6 were determined to have internal spread in their carbon (C) and N abundances, while Lindsay 113 was found to have a homogeneous distribution of helium abundance for its horizontal branch (HB) stars ($\delta Y \leq 0.01$ dex, Chantereau et al. 2019).

In this work, we dissect the 4 Gyr-old SMC cluster Lindsay 113, which is a low mass cluster located well below the minimum threshold mass for clusters with MPs. We aim to examine if its RGB exhibit any intrinsic broadening which can be explained by internal chemical variations among its RGB stars. Our work confirms that the observed width of the RGB of Lindsay

113 can be adequately explained by a SSP model, which disagrees with a recent study lead by [Martocchia et al. \(2019\)](#), however.

In Section 2 we will introduce our data reduction. We present our analysis approach and main results in Section 3. In Section 4 we will present the scientific implication and conclusions. We will also discuss the possible reason which leads to the disagreement between our result and that of [Martocchia et al. \(2019\)](#).

2. DATA REDUCTION

The observations were obtained with both the *HST*'s Ultraviolet and Visual Channel of the Wide Field Camera 3 (UVIS/WFC3) and the Advanced Camera for Surveys/Wide Field Channel (ACS/WFC). The UVIS/WFC3 images were observed through the F343N and F438W passbands (program ID: GO-15062, PI: N. Bastian). The ACS/WFC images (program ID: GO-9891, PI: G. F. Gilmore) are collected through the F555W (480s) and F814W (280s) passbands. The UVIS/WFC3 dataset includes three frames taken through the F343N passband, with exposure times of 540 s and 1065 s (twice), and three frames taken through the F438W passband, with exposure times of 128 s and 545 s (twice).

We used the specific photometric package designed for *HST* observations, the DOLPHOT2.0 ([Dolphin. 2011a,b, 2013](#)), to perform the point-spread-function (PSF) photometry to the ‘_flt’ and ‘_c0f’ frames. We used the corresponding WFC3 and ACS modules to deal with images taken from different observational channels. DOLPHOT2.0 has integrated functions of charge-transfer efficiency corrections and photometric calibration routines such as aperture and zeropoint corrections when applying measurement to *HST* observations, which make it a powerful tool for *HST* photometry.

After photometry, we have filtered the raw stellar catalogue by applying the following criteria: (1) identified by DOLPHOT2.0 as a ‘bright star’. (2) Not centrally saturated in any of each passband. (3) Sharpness is greater than -0.3 but less than 0.3 . (4) Crowding parameter is less than 0.5 mag. Finally we reach two stellar catalogues derived from the UVIS/WFC3 and ACS/WFC observations, with total number of “good stars” of 5,813 and 9,960, respectively. We then combine these two catalogues by cross-matching their spatial distributions, leading to a final stellar catalogue containing 4,380 stars.

3. MAIN RESULTS

3.1. Adopted Models

The color indices build with appropriate combination of ultraviolet, optical and near infrared magnitudes, is

an effective tool to search for MPs in GCs ([Larsen et al. 2014](#)). In particular, the F343N passband is sensitive to the N abundance as it includes the molecular absorption band of NH ($\sim 3370\text{\AA}$). The F438W contains the CH absorption band ($\sim 4300\text{\AA}$), thus it is sensitive to C abundance. A typical second population star, which is usually N-enriched and C-depleted, will be fainter in F343N but brighter in F438W than a normal star with the same stellar atmospheric parameters ($\log T_{\text{eff}}$, $\log g$, $[\text{Fe}/\text{H}]$). In addition, the temperature difference caused by different helium abundance between normal and enriched population stars could be revealed by the wide color baseline of F438W–F814W colors. We illustrate this principle in Figure 1 with the model spectra of one normal and one enriched star located at the base of the RGB with the stellar parameters of $T_{\text{eff}} = 5250\text{ K}$, $\log g = 3.5$, $[\text{Fe}/\text{H}] = -1.1$ dex and $V_t = 1.5\text{ km s}^{-1}$. Keeping the total CNO abundance constant (i.e., $\Delta[(\text{C} + \text{N} + \text{O})/\text{Fe}] = 0$ dex), the carbon, nitrogen and oxygen abundances of enriched stars are set to be $[\text{C}/\text{Fe}] = [\text{O}/\text{Fe}] = -0.4$ dex and $[\text{N}/\text{Fe}] = +0.8$ dex. Our model spectra are synthesized with the iSpec ([Blanco-Cuaresma et al. 2014; Blanco-Cuaresma 2019](#)) where the radial transfer code SPECTRUM ([Gray & Corbally 1994](#)) and the MARCS model atmosphere ([Gustafsson et al. 2008](#)) are adopted.

In Figure 2 we show three CMDs in different passbands of the Lindsay 113 cluster. We then fit these CMDs through the MESA Isochrone and Stellar Tracks (MIST; [Paxton et al. 2011, 2013, 2015; Choi et al. 2016; Dotter 2016](#)). As previously noticed by [Barker & Paust \(2018\); Li & de Grijs \(2019\)](#), we are not able to provide simultaneously a good fit to all CMDs. The poor fit is likely due to the uncertainties on the adopted extinction law in the SMC¹. We find the isochrone can fit the (F555W, F555W–F814W) CMD very well. However, the fitting deteriorates when the first passband becomes bluer. Because of this, in this work, we only focus on the width of the RGB rather than its position. Moreover, we adopt for Lindsay 113 the age, distance and metallicity inferred from the (F555W, F555W–F814W) CMD, where the effect of reddening is less evident, which are, $\log(t\text{ yr}^{-1}) = 9.64 \pm 0.02$ (4.37 ± 0.20 Gyr), $[\text{Fe}/\text{H}] = -1.15 \pm 0.10$ dex, $(m - M)_0 = 18.78 \pm 0.05$ mag and $E(B - V) = 0.05 \pm 0.01$ mag. The associated uncertainties were defined by the size of the adopted grids. We determined the best-fitting age by inspecting the relative position of the isochrone to the SGB. The metallicity was determined by the slope of the RGB. The best-fitting distance modulus, as well as the extinction value,

¹ MIST model sets the Milky Way extinction curve as the sole option when interpolate isochrones

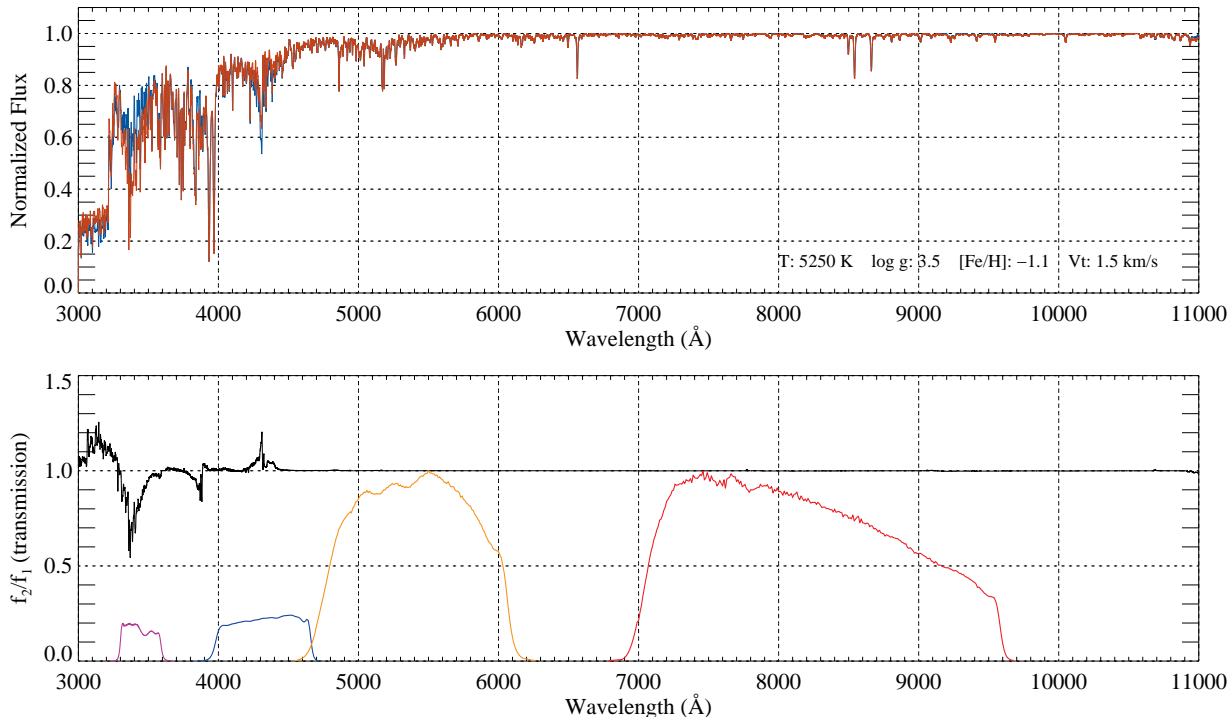


Figure 1. Top: Model spectra of different CNO composition. The blue spectrum represents the star of normal abundances, while the red one represents the star of enhanced nitrogen and depleted carbon and oxygen ($\Delta[\text{N}/\text{Fe}] = +0.8$ dex, $\Delta[\text{C}/\text{Fe}] = \Delta[\text{O}/\text{Fe}] = -0.4$ dex). The stellar parameters are indicated at the right-bottom corner. Bottom: Flux ratio and filter transmission curves used here (from left to right: F343N/WFC3, F438W/WFC3, F555W/WFC, F814W/WFC).

were defined by the position of the red clump (RC). For another two CMDs, the fitting of the isochrones to the positions of the RGB and the RC is our priority, because we are more interested in these parts rather than its MS. Our results are similar to those found in [Piatti \(2018\)](#); [Chantereau et al. \(2019\)](#).

3.2. Synthetic SSPs

Based on the best-fitting MIST isochrone, we simulated multi-bands photometry to compare with our observations. Possible effects other than the star-to-star chemical variations which may broaden the RGB include (i) photometric uncertainties and artifacts (e.g., cosmic rays, hot pixels), (ii) different distances of individual stars, (iii) differential reddening, and (iv) overlapped field stars with different ages and metallicities. The potential broadening of RGB caused by different stellar distances is negligible because of the large distance of the cluster. In principle, by using the artificial star technique, we can evaluate the effects of photometric uncertainties and artifacts. To do this, we have generated more than one million artificial stars (ASs) located on the best-fitting isochrone. We defined 10,000 sub-sample of ASs containing 100 stars each and added them to the images by using the appropriate PSF model

derived from real stars. These stars have been reduced by using the same method adopted for real stars. Our final artificial catalog contains 751,310 stars. We verified that most of the non-detected ASs are either faint stars or saturated objects. From these 751,310 stars, we randomly selected roughly the same number of artificial stars to the observation based on the observed luminosity function.

However, for the real observation, additional uncertainties may still occur due to multiple reasons. First, the PSF-fitting would never be perfect for real stars, as it would for the simulated ASs. Also, even there is no differential reddening effect, the photometric zero points would still exhibit spatial dependent variations due to the inaccuracies in the determination of the background and/or in the charge transfer efficiency correction. In principle, these effects are small but unpredictable. [Milone et al. \(2012\)](#) have compared the difference between the color spread of observed MS stars in GCs (with differential reddening corrected) with that of ASs. They find that the observed width of MS is about ~ 0.003 – 0.005 mag wider than the artificial MS, indicating an additional magnitude spread of 0.002 – 0.004 mag on average. In this work, we have also added additional noise of $\delta = 0.003$ mag in each passband. We argue that

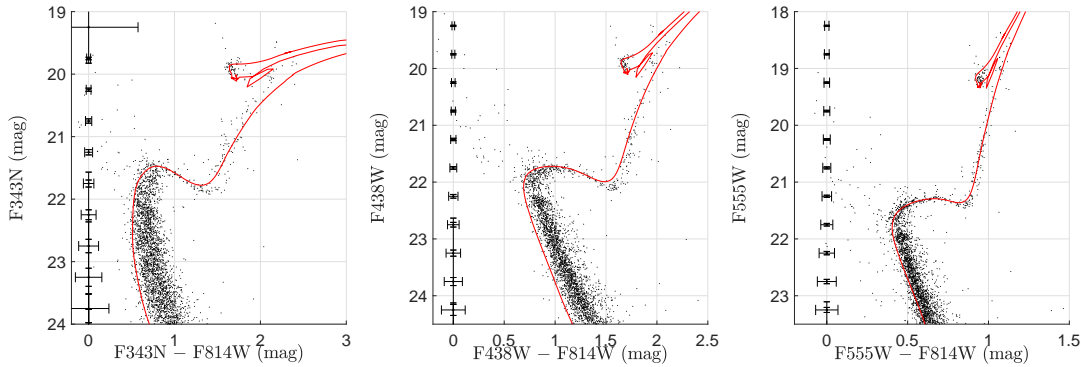


Figure 2. Lindsay 113 CMDs. (left) $F343N - F814W$ vs $F343N$; (middle) $F438W - F814W$ vs $F438W$; (right) $F555W - F814W$ vs $F555W$. Red lines are best-fitting isochrones. In each panel, average photometric uncertainties (corresponding to 90% confidence interval) are on the left side.

any conclusion on the presence of multiple populations in Lindsay 113 (or any other cluster) should account for these properties of ASs.

Recently [Martocchia et al. \(2019\)](#) conclude that the effect of differential reddening in this cluster is negligible. However, we do find that the observed patterns in the observed CMD are more dispersed than those of the ASs without differential reddening (even taken the additional noise into account as described above). We conclude that Lindsay 113 is indeed affected by differential reddening. This is the *major* difference between [Martocchia et al. \(2019\)](#) and this work. We will provide more details in Section 4.1 for this issue.

The effect of differential reddening was explored by comparing the simulated CMDs with the observational CMD in $F555W$ and $F814W$, because the effect of possible N spread will not significantly affect the photometry in these passbands. In addition, [Chantreau et al. \(2019\)](#) have concluded that the helium variation among Lindsay 113 stars is negligible. We find that the observed CMD is indeed more broadened in all parts (MS, SGB, RGB) than the simulated CMD without differential reddening. We then compare the width of the observed RGB with that of the simulation with differential reddening (see Section 3.3 for the identification of the RGB). We conclude that the degree of differential reddening is most likely $\delta E(B - V) = 0.005 \pm 0.002$ mag. Figure 3 shows the observed CMD (left) as well as three simulated CMDs with differential reddening degrees of $\delta E(B - V) = 0.0, 0.005, \text{ and } 0.01$ mag, respectively. From Figure 3, one can see that Lindsay 113 does not have an eMSTO, as expected ([Georgy et al. 2019](#)).

3.3. Statistical Analyses

Figure 4 illustrates how do we select RGB stars. We used the simulated CMDs in $F438W$ and $F555W$ in respect with $F814W$ to determine the regions occupied by

the majority of RGB stars. We determined the RGB selection boxes by examining their relative deviation to the ridgeline (for the simulated RGB, the ridgeline is the best-fitting isochrone). Only stars located in both selection boxes were considered RGB stars. This method has been used for minimizing the effect of field-star contamination ([Martocchia et al. 2017](#)). We have identified 67 candidates as member RGB stars.

We constructed a color index, $C_{F343N, F438W, F814W} = (F343N - F438W) - (F438W - F814W)$, to quantify the broadening of the RGB caused by chemical variations, which is similar to the index used in [Monelli et al. \(2013\)](#). This pseudo-color index is sensitive to unveil internal spread of C and N abundances ([Monelli et al. 2013; Martocchia et al. 2017](#)). We then compared the observed RGB in the $C_{F343N, F438W, F814W}$ versus $F438W$ diagram with that for artificial RGB. In Figure 5 we compare the observed CMD with eight simulated CMDs of SSPs derived from randomly-extracted ASs. We did not see any visible difference between the observation and simulations (SSPs). The analysis of a large sample of over 100 simulated CMDs confirm that the observed RGB width is consistent with the width expected from observational errors alone.

In Figure 6 we compared the $\Delta C_{F343N, F438W, F814W}$ distributions (histograms) of observed RGB with those of simulated CMDs. Here $\Delta C_{F343N, F438W, F814W}$ is defined as the relative deviation of $C_{F343N, F438W, F814W}$ for individual stars to their average $C_{F343N, F438W, F814W}$ of stars with similar magnitude. We find that the observed distribution of $\Delta C_{F343N, F438W, F814W}$ for RGB stars is well consistent with that of the simulations, i.e., SSPs. We have fitted the distributions of the pseudo-color index for both the observation and the average distributions of the simulated CMD, using a Gaussian profile. For the simulations, their average distribution of the

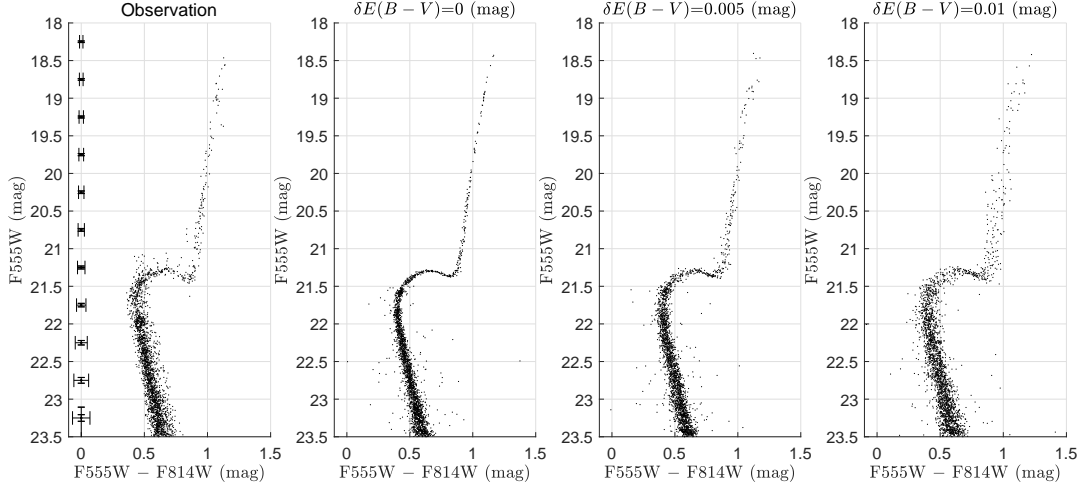


Figure 3. The observed CMD of Lindsay 113 with error bars (left) and simulated CMDs characterized by different degrees of differential reddening (as indicated by their titles). The added differential reddening was derived from a Gaussian distribution.

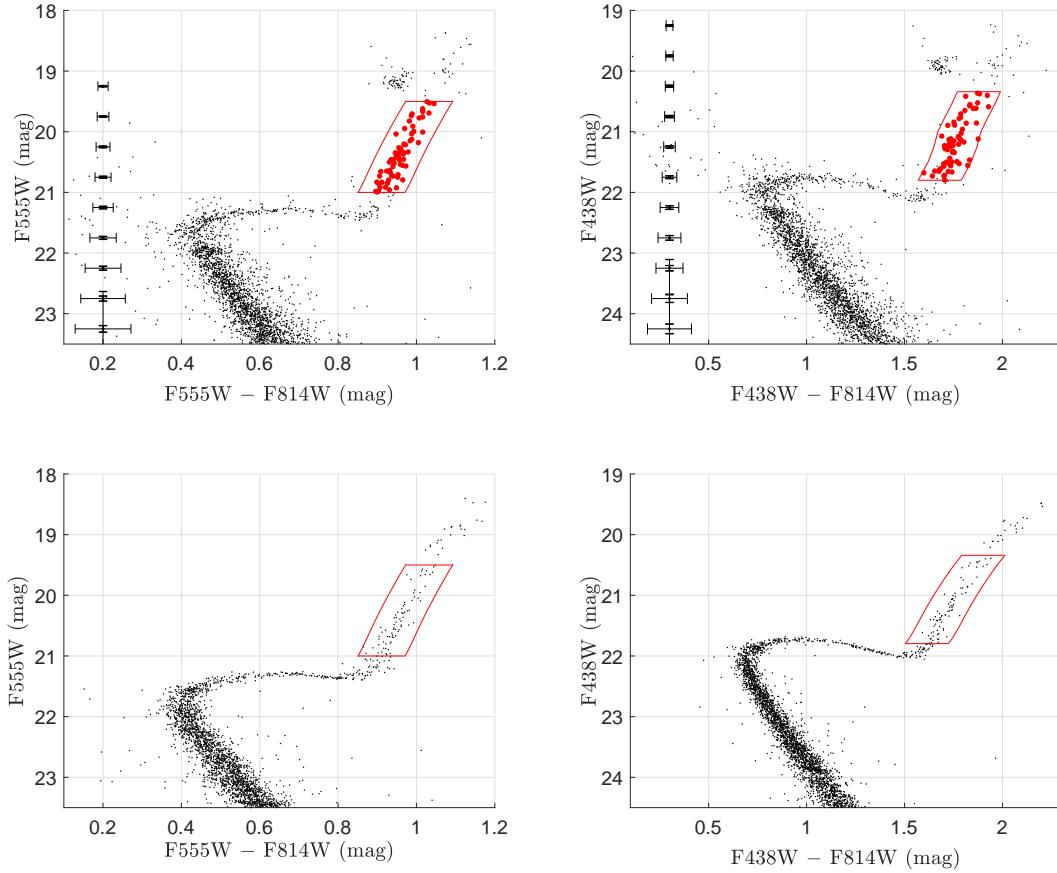


Figure 4. Identification of RGB stars from the observations (with error bars on the left side). Stars located in selection boxes of both CMDs involving F438W, F555W and F814W are member RGB stars. The selection boxes were determined based on the artificial CMDs (bottom panels).

$\Delta C_{F343N,F438W,F814W}$ can be described as follow,

$$P(\Delta C) = 0.34e^{-\left(\frac{\Delta C}{0.08}\right)^2}, \quad (1)$$

while for the observation, it is

$$P(\Delta C) = 0.38e^{-\left(\frac{\Delta C - 0.01}{0.07}\right)^2}, \quad (2)$$

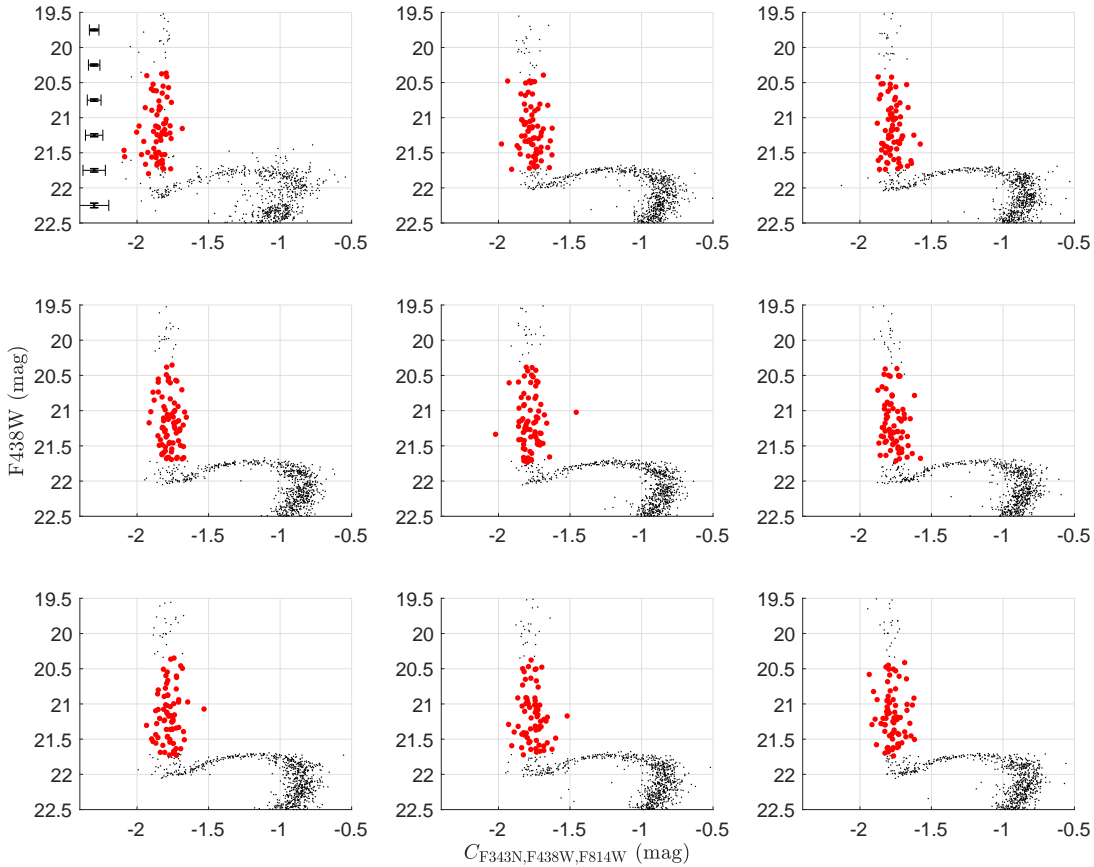


Figure 5. The $C_{F343N,F438W,F814W}$ vs. F_{438W} diagram for the observation with error bars (first row, left panel), the red dots are selected RGB stars. Other panels exhibit eight examples of simulated SSPs

this internal spread of the pseudo-color index (corresponding to a 68% confidence) for the observed RGB stars is $\sigma = 0.07 \pm 0.02 \text{ mag}^2$, which is consistent with the simulated SSPs ($\sigma = 0.08 \pm 0.02$). In this example we have used 5000 ASs. These results are shown in Figure 6.

For the analysis above, we compare the observed color distribution with the color distribution of ASs, by adding to ASs a reasonable amount of differential reddening. As an alternative, we also studied the color distribution of the RGB corrected for differential reddening and compared it with the color distribution of ASs. In this case we did not add any differential reddening to ASs, but only a reasonable error associated to the differential reddening.

To investigate the effect of differential reddening on the diagrams of Lindsay 113 we applied the method by

Milone et al. (2012) to the $F336W$ vs. $F336W - F814W$ CMD, which is the CMD that provides the wider color baseline. We selected a sample of ~ 1000 well-measured bright MS stars and derived the fiducial line. We derived for each star its residual from the fiducial, along the reddening line, and then corrected the star’s color and magnitude by the median residual of its 45 selected MS neighbors. As a result, we find that $\sim 97\%$ of stars in the field of view are affected by a reddening variation of $-0.016 \leq \Delta E(B - V) \leq 0.016 \text{ mag}$, while 68% of our sample have a differential reddening of $-0.006 \leq \Delta E(B - V) \leq 0.006$. This further supports that our previous adoption of $\delta E(B - V) = 0.005 \pm 0.002 \text{ mag}$ to the ASs is reasonable.

In Figure 7, we show the performance of our correction of differential reddening. We selected two subsamples with $\Delta E(B - V) > 0.005 \text{ mag}$ and $\Delta E(B - V) < -0.005 \text{ mag}$. We then plot their CMDs ($F336W$ vs. $F336W - F814W$) together (the left-top panel of Figure 7). One can see that stars with $\Delta E(B - V) > 0.005$

² The uncertainty was estimated by a bootstrap test.

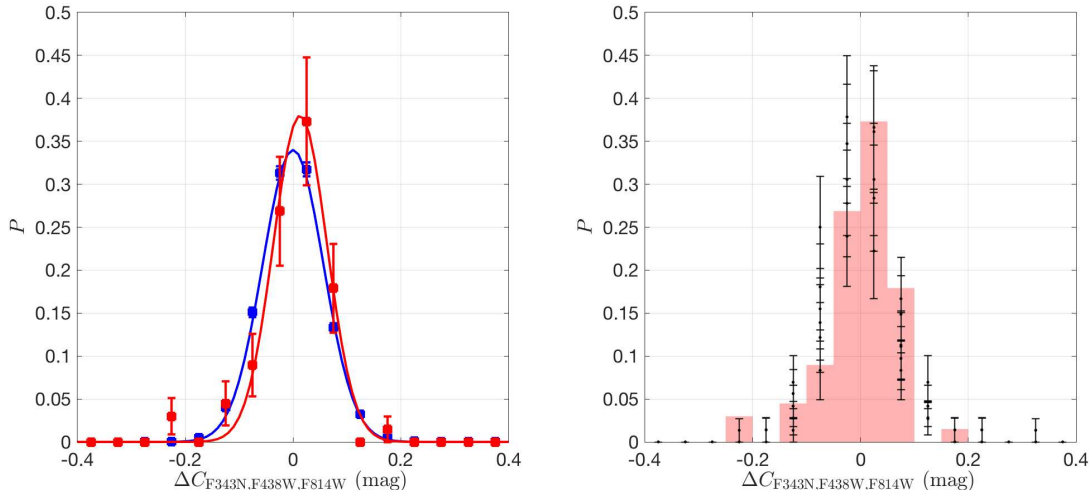


Figure 6. Left: the observed distributions of $\Delta C_{F343N,F438W,F814W}$ (red circles) versus that for the simulations (blue circles). The red and blue curves are their best fitting Gaussian curves. Right: the observed histogram for stars with different $\Delta C_{F343N,F438W,F814W}$. The black dots with error bars are the $\Delta C_{F343N,F438W,F814W}$ distributions for eight individual simulated samples (corresponds to Figure 5).

mag are indeed systematically redder than stars with $\Delta E(B - V) < -0.005$ mag. In the left-bottom panel of Figure 7, we show the same CMD with differential reddening corrected. As a result, we find that the color difference between these two subsamples disappears, and all parts of the CMD become much narrower than those of the raw CMD. In the right panel, we plot the differential reddening map in the whole field of view.

Because the method we used for correcting the differential reddening is still based on statistics, each value of differential reddening has associated an error of σ/N , where σ is the dispersion of the residuals of the N neighbors used for the correction. The average associated errors in our case is $\delta E(B - V) \sim 0.0026$ mag. Similar to previous analysis, in Figure 8 we show a comparison between the differential reddening corrected diagram for the observation and the ASs. The AS sample was incorporated with noise from photometric uncertainty, artifacts and position-dependent zero point, as well as the variations of PSF-fitting and reddening residuals. But in this case, it is free of differential reddening. We confirm that the observed RGB in the $C_{F343N,F438W,F814W}$ vs. F438W diagram becomes narrower and similar to that of ASs without differential reddening.

Similar to Figure 6, in Figure 9 we plot the distributions of $\Delta C_{F343N,F438W,F814W}$ for both the observed RGB stars with differential reddening corrected, and the ASs without differential reddening effect. Again, we used a single Gaussian function to fit these distributions: for the simulated ASs, the best fitting Gaussian function is

$$P(\Delta C) = 0.46e^{-\left(\frac{\Delta C}{0.06}\right)^2}, \quad (3)$$

and for the observation, it is

$$P(\Delta C) = 0.48e^{-\left(\frac{\Delta C}{0.06}\right)^2}, \quad (4)$$

For both the observation and the simulation, their RGB stars all exhibit an internal spread of the pseudo-color index of $\sigma = 0.06 \pm 0.02$ mag. Again, this result supports that there is no significant chemical variation among the RGB stars of Lindsay 113.

3.4. Constraint on the internal chemical variation

Using the MARCS model atmospheres (Gustafsson et al. 2008), based on the best fitting isochrone, we calculated the corresponding loci with different C, N and O abundances. We calculate the relative deviation between loci with $\Delta[N/Fe]=0.2, 0.4, 0.6$ and 0.8 dex to the standard isochrone. We then apply these deviations to the ridge-line of the observed RGB in the $C_{F343N,F438W,F814W}$ vs. F438W diagram. Finally we obtained four ridgelines for populations with abundance variations as introduced above. Based on these ridgelines, we simulated one SSP and four MPs with different $[N/Fe]$. For each simulated population, the number of stars is equal to the observation (readers can direct to our Figure 10 for a quick view).

To quantify the similarity between the observed and simulated distributions of the $C_{F343N,F438W,F814W}$, we have applied a two-sample KolmogorovSmirnov test (K-S test) to the observation and each simulation. For each run, the K-S test will return two values, H and P . The outcome of H depends on the null hypothesis that the two underlying distributions (the observation and tested simulation) are independent. If H returns

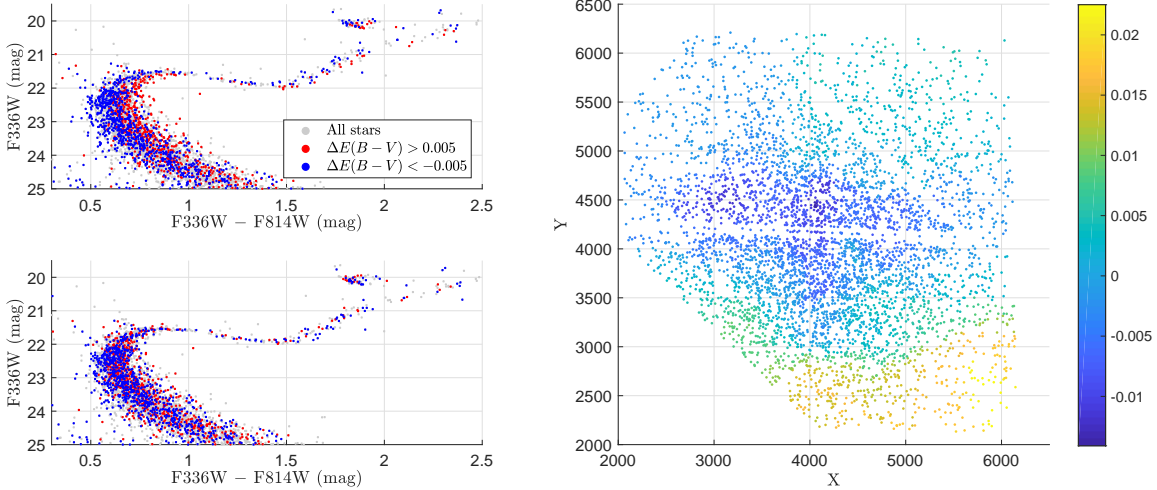


Figure 7. Left-top: CMDs of stars with $\Delta E(B - V) > 0.005$ mag and $\Delta E(B - V) < -0.005$ mag. Left-bottom: CMDs of stars with $\Delta E(B - V) > 0.005$ mag and $\Delta E(B - V) < -0.005$ mag, with differential reddening effect corrected. Right: the differential reddening map ($\Delta E(B - V)$ (mag)) for all stars.

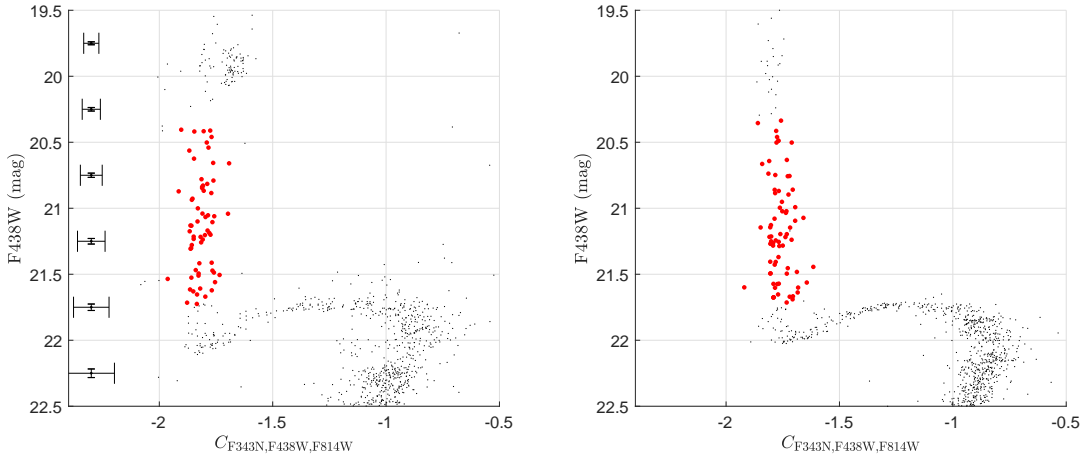


Figure 8. Similar to Figure 5, but the observed $C_{F343N,F438W,F814W}$ vs. $F438W$ diagram (left) was corrected for differential reddening. The same diagram for an example of ASs that is free of differential reddening, is presented in the right panel.

0, that means the null hypothesis is rejected, indicating that the observed and simulated $C_{F343N,F438W,F814W}$ are drawn from the same distribution. Otherwise, it returns 1. The P represents the probability that the two samples are drawn from the same underlying population. For an individual K-S test, typically when the P value is higher than 0.05, the null hypothesis is rejected.

To avoid the uncertainty caused by the small number statistics, for each simulation, we repeat the procedure 10,000 times. We then examine how many times the two-sample K-S test will return a $H=1$ and calculate the average P value for these 10,000 runs. Our results are summarized in Table 1.

Table 1. The outcomes of the two-sample K-S test between the observed and simulated $C_{F343N,F438W,F814W}$ distributions.

	$N(H = 1)^a$	\bar{P}
$\Delta[N/Fe]=0.0$ (SSP)	9084	0.31
$\Delta[N/Fe]=0.2$	8092	0.23
$\Delta[N/Fe]=0.4$	2403	0.04
$\Delta[N/Fe]=0.6$	94	2.6×10^{-3}
$\Delta[N/Fe]=0.8$	0	7.3×10^{-5}

^aWe have totally ran 10,000 times.

As shown in Table 1, we find that for models with $\Delta[N/Fe]=0.0$ or $\Delta[N/Fe]=0.2$, most runs (over 8000)

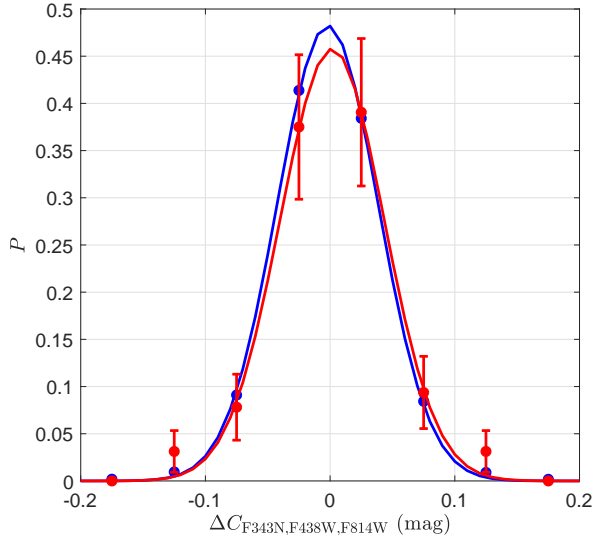


Figure 9. The same as the left panel of Figure 6, but the observed RGB stars have their differential reddening corrected (indicated by red circles), while the simulated ASs are differential reddening free (blue circles).

of the two-sample K-S test will report $H=1$. When increasing the internal nitrogen variation of models to $\Delta[\text{N}/\text{Fe}]=0.4$, the number of runs with $H=1$ sharply decrease to 2403, and their average P value also decreases to 0.04. For models with $\Delta[\text{N}/\text{Fe}]=0.6$ and 0.8, only 94 and zero runs will report $H=1$. Therefore we conclude that the internal chemical spread of the observed RGB stars is most likely $\Delta[\text{N}/\text{Fe}]\leq 0.2$. In Figure 10, we exhibit examples of the observed and simulated RGB in the $C_{\text{F}343\text{N},\text{F}438\text{W},\text{F}814\text{W}}$ vs. $\text{F}438\text{W}$ diagrams. Among these examples, only for models with $\Delta[\text{N}/\text{Fe}]=0.0$ and 0.2, the K-S test returns $H=1$. For other models with $\Delta[\text{N}/\text{Fe}]=0.4, 0.6$ and 0.8, the K-S test returns $H=0$.

4. DISCUSSION AND SUMMARY

4.1. A possible solution to the disagreement to *Martocchia et al. (2019)*

Recently *Martocchia et al. (2019)* have studied four intermediate-age clusters include Lindsay 113. In contrast to this work, they conclude that Lindsay 113 harbors MPs because of the observed broadening of the RGB in this cluster. Our work confirms the evidence of a color broadening in the RGB of Lindsay 113; however, our analysis suggests that such broadening is mostly due to differential reddening.

One reason that may explain the disagreement between this work and *Martocchia et al. (2019)* is that they have used a sample of RGB stars, which are less appropriate to correct the differential reddening. In fact,

the total number of stars from the base to the top of the RGB is only ~ 150 , that means for each particular star, they cannot find a sufficiently large number of nearby stars to study the average reddening in a small spatial cell. We suggest that the spatial resolution of their differential reddening map is poor, that might explain they claim that the effect of differential reddening effect is negligible. Indeed, as shown in Figure 3 and Figure 7, this effect is significant.

The differential reddening effect is important in particular for observations involving UV passbands. *Martocchia et al. (2019)* have studied the distribution of RGB stars in the color index of $C_{\text{F}343\text{N},\text{F}438\text{W},\text{F}336\text{W}}$ ³, for which two UV passbands (F336W and F343N) are involved. As a result, they find that the spread in this color index between the observed RGB stars and ASs is a little different, which are $\sigma = 0.041 \pm 0.003$ mag and $\sigma = 0.024$ mag.⁴ As shown in this work, the average differential reddening degree is most likely $\delta E(B-V)=0.005$ mag, which will lead to an additional uncertainties of $\delta F336W \approx \delta F343N = 1.6 \times 3.1 \times \delta E(B-V) = 0.025$ mag, and $\delta F438W = 1.3 \times 3.1 \times \delta E(B-V) = 0.02$ mag. These uncertainties will finally combine into uncertainty of $\delta C_{\text{F}336\text{W},\text{F}438\text{W},\text{F}343\text{N}} = 0.045$ mag. The differential reddening is indeed important.

Using the same method and database utilized in *Martocchia et al. (2019)*, we calculated the $\Delta C_{\text{F}336\text{W},\text{F}438\text{W},\text{F}343\text{N}}$ distribution for a differential reddening free AS sample. The standard deviation of these artificial RGB stars is $\delta(C_{\text{F}336\text{W},\text{F}438\text{W},\text{F}343\text{N}}) = 0.027$ mag, which is consistent with *Martocchia et al. (2019)*. We then assume a degree of $\delta E(B-V) = 0.005$ mag for all ASs, after that the artificial RGB becomes wider with $\delta(C_{\text{F}336\text{W},\text{F}438\text{W},\text{F}343\text{N}}) = 0.052$ mag, which fully explains the observed width of RGB stars in $C_{\text{F}336\text{W},\text{F}438\text{W},\text{F}343\text{N}}$ (0.041 ± 0.003 mag). Our result is presented in Figure 11.

Therefore, we suggest that not taking differential reddening into account might hamper the conclusion about Lindsay 113 made by *Martocchia et al. (2019)*. No evidence of significant chemical variation can be detected through this photometric database.

4.2. Scientific Implications

In analogy to *Martocchia et al. (2018)*, we summarize clusters with and without MPs into the age–mass diagram in Figure 12. There is a clear age boundary located between 1.8 Gyr and 2.0 Gyr, as indicated by the verti-

³ $(\text{F}343\text{N} - \text{F}438\text{W}) - (\text{F}438\text{W} - \text{F}336\text{W})$

⁴ here σ indicates the standard deviation of $C_{\text{F}343\text{N},\text{F}438\text{W},\text{F}336\text{W}}$ for RGB stars.

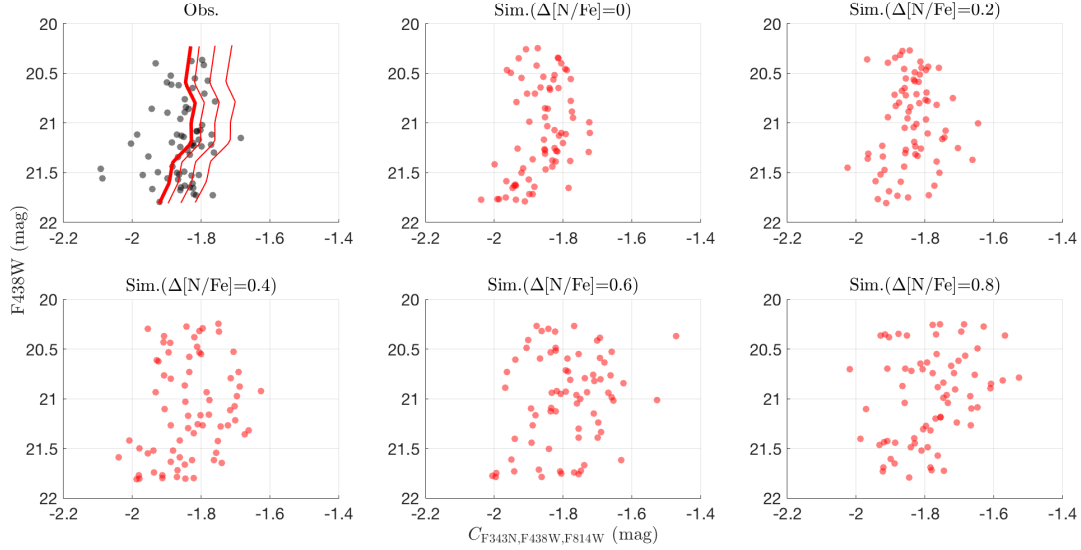


Figure 10. The observed (top-left panel) and the simulated RGB stars with different CNO abundances in the $C_{F343N,F438W,F814W}$ versus $F438W$ diagram. The thick solid line is the best fitting ridgeline to the observation. From left to right, the thin solid lines are loci with $\Delta[N/Fe]=0.2$, 0.4 and 0.6 , respectively. Only for models with $\Delta[N/Fe]=0.0$ and 0.2 (top-middle and top-right), the two-sample K-S test will report that the simulated RGB stars have their $C_{F343N,F438W,F814W}$ distributions similar to the observation (over 80% of simulations have reproduced the observation). For $\Delta[N/Fe]=0.4$, only $\sim 24\%$ of simulations can reproduce the observation. For $\Delta[N/Fe]=0.6$, this ratio rapidly decreases to $\sim 1\%$ (see Table 1)

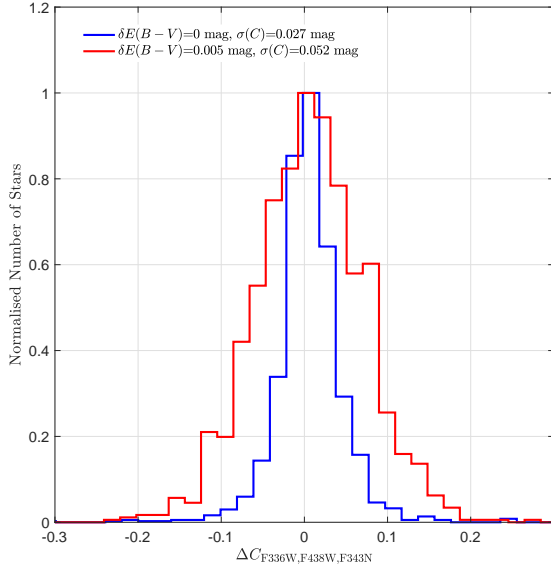


Figure 11. The $\Delta C_{F336W,F438W,F343N}$ distribution for artificial RGB stars with/without differential reddening (red/blue histograms).

cal dashed line. All clusters younger than this age range do not exhibit MPs, while most of their older counterparts do. For clusters between 2 to 10 Gyr, it seems that low mass clusters (less massive than $\sim 50,000 M_{\odot}$, horizontal dashed line) do not have MPs. However, it

remains quite uncertain because the number of studied stars in these clusters are small (Terzan 7, Palomar 12, Tautvaišienė et al. 2004; Sbordone et al. 2007), for which only three and five stars were studied through high-resolution spectra. For Milky Way GCs, only one cluster, Ruprecht 106 (the arrow in Figure 12 indicates its position in the mass-age plane), lacks MPs, as reported by Villanova et al. (2013) based on studies of nine member stars. This work is verified recently by Dotter et al. (2018) as well. However, because MPs have been detected in lower mass GCs (e.g., Bragaglia et al. 2017), it seems Rup 106 does not set a strong constraint on the mass limitation for the presence of MPs. Future studies of a larger sample of stars are essential for determining if there is a mass boundary for evolved clusters to harbor MPs.

In this paper, the photometric appearance of the intermediate-age (~ 4.4 Gyr), low mass ($\sim 23,000 M_{\odot}$) cluster, Lindsay 113, was analyzed. We have studied its RGB morphology in the diagram of $F438W$ versus $C_{F343N,F438W,F814W}$, an effective tool which can unveil significant variations in C and N among RGB stars. We have carefully corrected the effect of photometric uncertainties, artifacts, and potential differential reddening. We do not find apparent broadening of the RGB when comparing with that of simulated SSPs. Our observation is consistent with a model characterized by internal C and N abundances not exceeding $\Delta[C/Fe]=-0.1$ dex

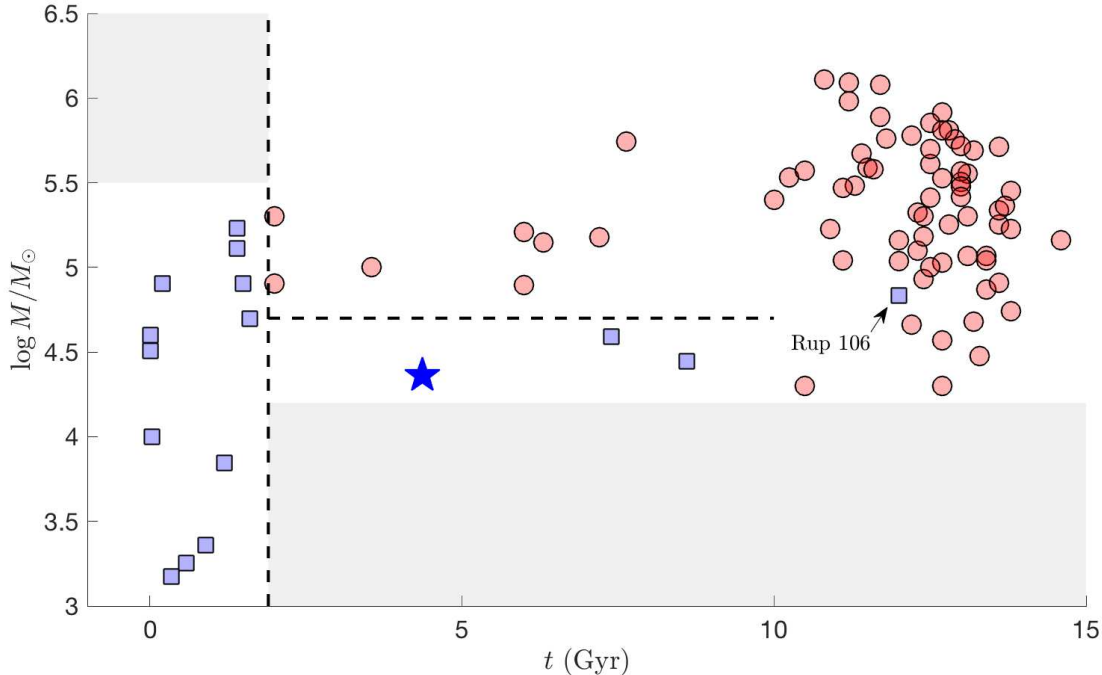


Figure 12. The age-mass plane for clusters with and without MPs (red circles and blue squares), and Lindsay 113 (the blue pentagram). The vertical and horizontal dashed lines indicate the possible age and mass boundary which may define the presence of MPs. Grey areas were the suggested searching parameter space for clusters in future studies. Data were obtained from [McLaughlin & van der Marel \(2005\)](#); [Baumgardt et al. \(2013\)](#); [Krause et al. \(2016\)](#).

and $\Delta[\text{N}/\text{Fe}] = 0.2$ dex. The noise contributed by photometric uncertainties, artifacts and differential reddening, as well as small number stochastic can adequately explain the observed width of the RGB.

The lack of MPs in Lindsay 113 provides solid evidence which indicates that clusters masses may still play a role on the presence of MPs, at least it defines the strength of the chemical spread among their member stars. Our result is in apparent contrast to the massive counterpart of Lindsay 113, NGC 2121: using the same method, [Li & de Grijs \(2019\)](#) conclude that NGC 2121 would harbor an internal N spread of ~ 0.5 dex.

Our result is further supported by the fact that Lindsay 113 lacks an apparent helium variation among its RC stars ([Chantereau et al. 2019](#)). Detail studies based on high-resolution abundances for individual stars would be essential to define whether this cluster is SSP. Studying this cluster in passbands of shorter wavelength (i.e., F275W at UVIS/WFC3) would provide additional evidence regards whether this cluster is a SSP, because MPs would exhibit variation in Oxygen (O) that can be observed through the OH molecular absorption at $\sim 2800\text{\AA}$ (e.g. [Milone et al. 2017](#)).

It would be interesting to study stellar populations in younger (≤ 2 Gyr) and massive ($\geq \text{few} \times 10^5 M_\odot$) clusters, as well as older (≥ 2 Gyr) but low mass ($\geq 30,000 M_\odot$)

clusters, as indicated by the grey areas in the age-mass plane (Figure 12). However, the Milky Way and its nearby satellite galaxies lack super young massive clusters, therefore to shed light on the MPs problem, we need next-generation telescopes to observe distant star forming galaxies. As an example, [Smith et al. \(2006\)](#) have detected five supermassive cluster candidates in the M82 galaxy, one of which has an estimated mass of over $10^6 M_\odot$ and an age of only ~ 6 Myr. To resolve individual RGB stars in clusters at this distance, an at least 8-meter UV-optical space telescope is required. However, current ground-based telescopes with the equivalent aperture (such as the Very Large Telescope) would suffer problems in adaptive optics when correcting the atmospheric turbulence at this short wavelength. Therefore, a more feasible direction is to explore stellar populations among those older, low mass clusters. The Magellanic Clouds already have a handful of these clusters (e.g., NGC 2193, [Baumgardt et al. 2013](#)). However, one problem is that these low mass clusters may not have a well-populated RGB because of the small number of stars, making the photometric method problematic. Overall, a combination of both the photometric and spectroscopic methods is essential. Another feasible project is to explore whether the young and intermediate-age clusters would have O variations

among their MK dwarfs. These O enhanced, late-type stars will exhibit strong absorption bands from the H₂O molecules, which can be detected in near-Infrared passbands. However, given these low mass dwarfs are extremely faint in these distant clusters, only the next-generation telescopes such as the *James Webb Space Telescope* or the *projected Extremely Large Telescope* can obtain a high signal to noise ratio measurements.

We thank the anonymous reviewer for their helpful comments and suggestions. C. L. acknowledges support from the one-hundred-talent project of Sun Yat-Sen

University. C. L. and Y. W. were supported by the National Natural Science Foundation of China under grants 11803048. Y. W. acknowledges the support by China Postdoctoral Science Foundation, and the Young Researcher Grant of National Astronomical Observatories, Chinese Academy of Sciences.

Facilities: *Hubble Space Telescope* (UVIS/WFC3 and ACS/WFC)

Software: DOLPHOT2.0 (DOLPHIN. 2011A,B, 2013) iSpec (Blanco-Cuaresma et al. 2014; Blanco-Cuaresma 2019)

REFERENCES

- Barker, H., & Paust, N. E. Q. 2018, *PASP*, 130, 034204
- Bastian, N., & Strader, J. 2014, *MNRAS*, 443, 3594
- Bastian, N., Cabrera-Ziri, I., & Salaris, M. 2015, *MNRAS*, 449, 3333
- Bastian, N., & Lardo, C. 2018, *ARA&A*, 56, 83
- Baumgardt, H., Parmentier, G., Anders, P., & Grebel, E. K. 2013, *MNRAS*, 430, 676
- Bekki, K. 2019, *A&A*, 622, A53
- Bell, R. A., Dickens, R. J., & Gustafsson, B. 1979, *ApJ*, 229, 604
- Blanco-Cuaresma, S., Soubiran, C., Heiter, U., & Jofré, P. 2014, *A&A*, 569, A111
- Blanco-Cuaresma, S. 2019, *MNRAS*, 486, 2075
- Bragaglia, A., Carretta, E., D’Orazi, V., et al. 2017, *A&A*, 607, A44
- Briley, M. M., Bell, R. A., Smith, G. H., & Hesser, J. E. 1989, *ApJ*, 341, 800
- Cannon, R. D., Croke, B. F. W., Bell, R. A., Hesser, J. E., & Stathakis, R. A. 1998, *MNRAS*, 298, 601
- Carretta, E., Bragaglia, A., Gratton, R. G., et al. 2009, *A&A*, 505, 117
- Carretta, E., Bragaglia, A., Gratton, R. G., et al. 2010, *A&A*, 516, A55
- Cavallo, R. M., Sweigart, A. V., & Bell, R. A. 1996, *ApJL*, 464, L79
- Cavallo, R. M., Sweigart, A. V., & Bell, R. A. 1998, *ApJ*, 492, 575
- Chantereau, W., Salaris, M., Bastian, N., & Martocchia, S. 2019, *MNRAS*, 484, 5236
- Choi, J., Dotter, A., Conroy, C., et al. 2016, *ApJ*, 823, 102
- Dotter, A. 2016, *ApJS*, 222, 8
- Cordoni, G., Milone, A. P., Marino, A. F., et al. 2018, *ApJ*, 869, 139
- Dalessandro, E., Lapenna, E., Mucciarelli, A., et al. 2016, *ApJ*, 829, 77
- D’Antona, F., Milone, A. P., Tailo, M., et al. 2017, *Nature Astronomy*, 1, 0186
- Decressin, T., Meynet, G., Charbonnel, C., Prantzos, N., & Ekström, S. 2007, *A&A*, 464, 1029
- D’Ercole, A., Vesperini, E., D’Antona, F., McMillan, S. L. W., & Recchi, S. 2008, *MNRAS*, 391, 825
- de Mink, S. E., Pols, O. R., Langer, N., & Izzard, R. G. 2009, *A&A*, 507, L1
- Dolphin A., DOLPHOT/WFC3 user’s guide, version 2.0. <http://americano.dolphinim.com/dolphin/dolphotWFC3.pdf>
- Dolphin A., DOLPHOT/WFPC2 user’s guide, version 2.0. <http://americano.dolphinim.com/dolphot/dolphotWFPC2.pdf>
- Dolphin A., DOLPHOT user’s guide, version 2.0. <http://americano.dolphinim.com/dolphot/dolphot.pdf>
- Dotter, A., Milone, A. P., Conroy, C., Marino, A. F., & Sarajedini, A. 2018, *ApJL*, 865, L10
- Dupree, A. K., Dotter, A., Johnson, C. I., et al. 2017, *ApJL*, 846, L1
- For, B.-Q., & Bekki, K. 2017, *MNRAS*, 468, L11
- Georgy, C., Charbonnel, C., Amard, L., et al. 2019, *A&A*, 622, A66
- Gray, R. O., & Corbally, C. J. 1994, *AJ*, 107, 742
- Gustafsson, B., Edvardsson, B., Eriksson, K., et al. 2008, *A&A*, 486, 951
- Hollyhead, K., Martocchia, S., Lardo, C., et al. 2019, *MNRAS*, 484, 4718
- Hong, J., de Grijs, R., Askar, A., et al. 2017, *MNRAS*, 472, 67
- Jiang, D., Han, Z., & Li, L. 2014, *ApJ*, 789, 88
- Krause, M. G. H., Charbonnel, C., Bastian, N., & Diehl, R. 2016, *A&A*, 587, A53
- Lagioia, E. P., Milone, A. P., Marino, A. F., & Dotter, A. 2019, *ApJ*, 871, 140

- Larsen, S. S., Brodie, J. P., Grundahl, F., & Strader, J. 2014, *ApJ*, 797, 15
- Letarte, B., Hill, V., Jablonka, P., et al. 2006, *A&A*, 453, 547
- Li, C., de Grijs, R., Deng, L., et al. 2016, *Nature*, 529, 502
- Li, C., de Grijs, R., Deng, L., & Milone, A. P. 2017, *ApJ*, 844, 119
- Li, C., & de Grijs, R. 2019, *ApJ*, 876, 94
- Marino, A. F., Villanova, S., Piotto, G., et al. 2008, *A&A*, 490, 625
- Marino, A. F., Milone, A. P., Piotto, G., et al. 2009, *A&A*, 505, 1099
- Marino, A. F., Przybilla, N., Milone, A. P., et al. 2018, *AJ*, 156, 116
- Marino, A. F., Milone, A. P., Casagrande, L., et al. 2018, *ApJL*, 863, L33
- Martocchia, S., Bastian, N., Usher, C., et al. 2017, *MNRAS*, 468, 3150
- Martocchia, S., Cabrera-Ziri, I., Lardo, C., et al. 2018, *MNRAS*, 473, 2688
- Martocchia, S., Dalessandro, E., Lardo, C., et al. 2019, *MNRAS*
- McLaughlin, D. E., & van der Marel, R. P. 2005, *ApJS*, 161, 304
- Milone, A. P., Bedin, L. R., Piotto, G., & Anderson, J. 2009, *A&A*, 497, 755
- Milone, A. P., Piotto, G., Bedin, L. R., et al. 2012, *A&A*, 540, A16
- Milone, A. P., Piotto, G., Renzini, A., et al. 2017, *MNRAS*, 464, 3636
- Milone, A. P., Marino, A. F., Renzini, A., et al. 2018, *MNRAS*, 481, 5098
- Monelli, M., Milone, A. P., Stetson, P. B., et al. 2013, *MNRAS*, 431, 2126
- Mucciarelli, A., Origlia, L., Ferraro, F. R., & Pancino, E. 2009, *ApJL*, 695, L134
- Mucciarelli, A., Dalessandro, E., Ferraro, F. R., Origlia, L., & Lanzoni, B. 2014, *ApJL*, 793, L6
- Niederhofer, F., Bastian, N., Kozhurina-Platais, V., et al. 2017, *MNRAS*, 465, 4159
- Pancino, E., Romano, D., Tang, B., et al. 2017, *A&A*, 601, A112
- Paxton, B., Bildsten, L., Dotter, A., et al. 2011, *ApJS*, 192, 3
- Paxton, B., Cantiello, M., Arras, P., et al. 2013, *ApJS*, 208, 4
- Paxton, B., Marchant, P., Schwab, J., et al. 2015, *ApJS*, 220, 15
- Piatti, A. E. 2018, *AJ*, 156, 206
- Pilachowski, C. A., Sneden, C., Kraft, R. P., & Langer, G. E. 1996, *AJ*, 112, 545
- Piotto, G., Milone, A. P., Bedin, L. R., et al. 2015, *AJ*, 149, 91
- Piotto, G., Bedin, L. R., Anderson, J., et al. 2007, *ApJL*, 661, L53
- Sbordone, L., Bonifacio, P., Buonanno, R., et al. 2007, *A&A*, 465, 815
- Smith, L. J., Westmoquette, M. S., Gallagher, J. S., et al. 2006, *MNRAS*, 370, 513
- Sun, W., de Grijs, R., Deng, L., & Albrow, M. D. 2019, *ApJ*, 876, 113
- Sweigart, A. V., & Mengel, J. G. 1979, *ApJ*, 229, 624
- Tautvaišienė, G., Wallerstein, G., Geisler, D., Gonzalez, G., & Charbonnel, C. 2004, *AJ*, 127, 373
- Villanova, S., Piotto, G., King, I. R., et al. 2007, *ApJ*, 663, 296
- Villanova, S., Geisler, D., Carraro, G., Moni Bidin, C., & Muñoz, C. 2013, *ApJ*, 778, 186
- Wang, Y., Primas, F., Charbonnel, C., et al. 2017, *A&A*, 607, A135
- Yang, W., Bi, S., Meng, X., & Liu, Z. 2013, *ApJ*, 776, 112
- Zhang, H., de Grijs, R., Li, C., & Wu, X. 2018, *ApJ*, 853, 186